Nanoscale

Accepted Manuscript

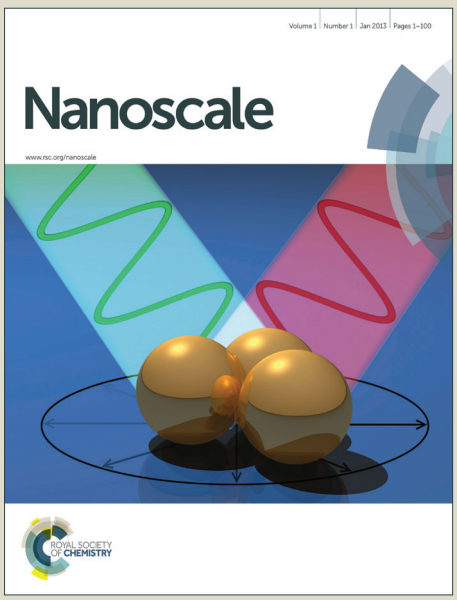

ROYAL SOCIETY OF CHEMISTRY

www.rsc.org/nanoscale

Cite this: DOI: 10.1039/c0xx00000x

www.rsc.org/xxxxxx

ARTICLE TYPE

Artificial Photosynthesis on Tree Trunks Derived Alkaline Tantalates with Hierarchical Anatomy: Towards CO_2 Photo-fixation into CO and CH_4

Han Zhou [a,d], Peng Li [a,b], Jianjun Guo [a,b], Runyu Yan [d], Tongxiang Fan [d], Di Zhang [d], and Jinhua Ye * [a,b,c]

Received (in XXX, XXX) Xth XXXXXXXXX 20XX, Accepted Xth XXXXXXXXX 20XX
DOI: 10.1039/b000000x

Artificial photosynthesis, that is photochemical fixation and recycling CO_2 back to hydrocarbon fuels from sunlight and water, is both a great challenge and an opportunity that, if realized, could have a revolutionary impact on our energy system. Herein, we demonstrate one of the first examples using biomass derived hierarchical porous photocatalysts for CO_2 photo-fixation into sustainable hydrocarbon fuels. A generic means is put forward to build a series of alkaline tantalates $MTaO_3$ (M=Li, Na, K) with hierarchical anatomy from macro- to nanoscales using activated carbonized tree trunks as templates. Artificial photosynthesis is carried out on $MTaO_3$ series using only artificial sunlight, water, and carbon dioxide as inputs to produce carbon monoxide and methane as the main outputs. The CO_2 photo-fixation performance can be enhanced by introduction of a macropore network, mainly due to the enhanced light transfer and faster gas diffusion. The research provides prototype models to integrate individual nanoscale components into higher level macroscopic artificial photosynthetic systems for better solar-to-fuel conversion efficiencies. This work would have potential significance for the ultimate construction towards "artificial trees" and provide envisions creating "forests" of these CO_2-capturing artificial trees to remove carbon dioxide from the atmosphere and convert it into sustainable fuels.

Introduction

The significant rise in atmospheric CO_2 levels because of the combustion of hydrocarbon fuels has generated worldwide concern. Among various CO_2 sequestration technologies, a compelling approach, normally known as artificial photosynthesis, is photochemical fixation and recycling CO_2 back to hydrocarbon fuels (e.g. CO, CH_4, CH_3OH, etc.) from sunlight and water, which are both a great challenge and an opportunity that, if realized, could have a revolutionary impact on our energy system [1-5]. Since the first report on the photo-fixation of CO_2 in 1978 [6], tremendous efforts have been devoted to developing new promising photocatalysts and to modifying the photocatalysts for enhanced efficiency [7-9]. In particular, some multi-metallic catalysts such as Zn_2GeO_4, [10,11] $ZnGa_2O_4$, [12,13] $NaNbO_3$, [14] Zn_2SnO_4, [15] Bi_2WO_6 [16,17] and so forth are very attractive in recent years due to their wide band gaps with high reduction potentials. However, up to now materials that are active for CO_2 photo-fixation reported are still very limited. Tantalates exhibit high photocatalytic performance because tantalates possess conduction bands at a more negative position than that of titanates, so a variety of mixed metal oxides containing closed-shell Ta^{5+} transition-metal ions have been studied recently [18,19]. As a typical example, alkaline tantalates $MTaO_3$ (M=Li, Na, K) show high activities for water splitting [18,19]. Therefore, they are likely to be promising for CO_2 photoreduction. However, in general, these tantalates are synthesized *via* a conventional solid-state reaction or polymerized complex method at high temperatures, leading to rather low porosity and low surface area which restrict their performance, especially for the gas-involved reactions.

Morphology control strategy has been an effective and versatile approach for promoting CO_2 photo-fixation activities [20], involving the construction of nanostructures [10,21,22], micro/mesoporous structures [11,12], hollow structures [23-25], metal-organic frameworks (MOFs) [26] with highly porous cavities and so forth. In recent years, materials with hierarchical porous anatomy have been a hot research area and are widely used in catalysis areas [27-29]. This is because materials with hierarchical porosity can provide from macro to nanolength scales of pores for reaction, interfacial transport, or dispersion of active sites and shorten diffusion paths or reduce diffusion [27,28]. However, to date there are few reports about the oriented design, controlled synthesis and ultimate application of hierarchically porous materials for CO_2 photo-fixation. Furthermore, there is no

report so far on the general synthesis of alkaline tantalates with well-defined hierarchical porous anatomy.

In green plants, leaves are well-known as the main photosynthetic organs. Tree trunks, as a main part of trees function as water/mineral transportation pathways for leaves' photosynthesis. They exhibit a hierarchically built anatomy which act as the central "plumbing system" in a tree, forming a network of tubes as transportation paths with three-dimensional (3D) high hierarchically porosity and high system connectivity that carries water and minerals up from the roots to the leaves, and sugar from the leaves down to the branches, trunk, and roots. The most distinct morphology feature of tree trunks, is the open porous system of the tracheidal cells which provide the transportation path for water in the living wood and yield an uniaxial pore structure with anisotropic mechanical properties [30]. Furthermore, tree trunk has a rather high surface area up to hundreds m^2 g^{-1}. Thus, such hierarchical anatomy would be a potential candidate for the directed synthesis of hierarchical systems.

Herein, we demonstrate one of the first examples using biomass derived hierarchical porous catalysts for CO_2 photo-fixation into sustainable hydrocarbon fuels. A generic means is put forward to build a series of alkaline tantalates $MTaO_3$ (M=Li, Na, K) with hierarchical anatomy using activated carbonized tree trunks as templates. Artificial photosynthesis is carried out on $MTaO_3$ series using only artificial sunlight, water, and carbon dioxide as inputs to produce carbon monoxide and methane as the main outputs. The CO_2 photo-fixation performance can be enhanced by introduction of a macropore network, due to the enhanced light transfer and faster gas diffusion in hierarchical meso/macroporous systems. The research provides prototype models to integrate individual functional components into higher level macroscopic artificial photosynthetic systems for better solar-to-fuel conversion efficiencies. This work would have potential significance for the ultimate construction towards "artificial trees" or "artificial plants" and provide envisions creating "forests" of these CO_2-capturing artificial trees to remove carbon dioxide from the atmosphere and convert it into sustainable fuels.

Experimental Section

Pretreatment/activation of wood template: First, the specimens ($10\times10\times10$ mm^3) of White Pine woods were boiled in 5% ammonia solution overnight to remove the wood extractive compounds like organic acid and lipid so that the connectivity of the wood's pores can be increased for better precursor's soakage. The extracted wood templates were washed by deionized water completely. The wood was calcined at 400°C for 2h under N_2 atmosphere, with a heating rate of 1°C min^{-1}. The obtained carbonized wood was infiltrated in NaOH solution (mass ratio of carbonized wood: NaOH=1:4) at 80°C until the water solution was evaporated. For the synthesis of $KTaO_3$ and $LiTaO_3$, KOH and LiOH solutions were used instead respectively. Then the carbonized wood was calcined at 600°C for 2 h under N_2 atmosphere, with a heat rate of 1 °C min^{-1}. The obtained activated carbonized wood was dispersed in DI water and then concentrated HNO_3 (70%) was added drop by drop until the solution was acidic. Then the wood was washed with DI water and ethanol completely and dried in vacuum oven at 60°C overnight.

Synthesis of $MTaO_3$ (M=Li, Na, K) from the activated carbonized wood: Typically, for the synthesis of $NaTaO_3$, 10 mM sodium acetate was first dissolved in 100 mL anhydrous ethanol and stirred for 30 mins. Then stoichiometric amounts of tantalum ethoxide that dissolved in 100 mL 2-Methoxyethanol solution was added into the above solution and stirred for 2 hrs. 1.0 g Activated carbonized wood was immersed into the precursor solution and infiltrated under vacuum at 50 °C for 8 hrs. Excess precursor solution was washed away by anhydrous ethanol four times. The as-obtained infiltrated carbonized wood was dry at room temperature overnight and then calcined at 550°C for 10 h under O_2 atmosphere, with a heat rate of 1 °C min^{-1}. For the synthesis of $KTaO_3$ and $LiTaO_3$, potassium acetate and lithium acetate were used instead of sodium acetate, respectively.

Loading the co-catalysts: The loading of Au was also performed by a precipitation method. The precipitation procedure was done at 343 K and pH 9 for 4 h with 1 wt % $HAuCl_4 \cdot 3H_2O$ as the Au source, using (0.2 M) NaOH to maintain the pH constant. The catalyst was then recovered, filtered, washed with deionized water, and dried at 373 K overnight. Finally, the powder was calcined at 473 K in air for 4 h.

CO_2 Photoreduction Measurements: The CO_2 photoreduction experiments were carried out in a gas closed circulation system with an upside window (Supporting Information, Figure S1). The catalyst (50 mg) was dispersed on a small glass cell with a base area of 8.1 cm^2 and then located in a Pyrex reaction cell. After that, 2 mL of distilled water was added into the gas closed reaction system. The volume of the reaction system is around 390 mL. The whole system was then evacuated and filled with 80 kPa of pure CO_2 gas. The light source was a 200 W Hg-Xe arc lamp (ILC Technology, CERMAX LX-300). The organic products were sampled and measured with a gas chromatograph (GC-14B, Shimadzu) equipped with a flame ionization detector (FID) according to the standard curves. For CH4 detection, PEG-1000 chromos column was used. For CO detection, Propark Q column was used. The H_2 and O_2 evolution was measured with an online gas chromatograph (GC-8A, Shimadzu) with a TCD detector according to the standard curve.

Characterization: The crystal structure of samples was determined with an X-ray diffractometer (Rint-2000, Rigaku Co., Japan) with Cu Kα radiation. The diffuse reflection spectra were measured with an integrating sphere equipped UV−visible recording spectrophotometer (UV-2500PC, Shimadzu Co., Japan) using $BaSO_4$ as a reference, and the optical absorptions were converted from the reflection spectra according to the Kubelka−Munk equation. Scanning Electron Microscopy (SEM) images were recorded to observe the morphology with scanning electron microscope (JEOL 6700F field emission scanning electron microscope). Transmission electron microscopy images and high-resolution images were recorded with a field emission transmission electron microscope (2100F, JEOL Co., Japan) operated at 200 kV. The specific surface areas were determined with a surface-area analyzer (BEL Sorp-II mini, BEL Japan Co.,

Japan) by the Brunauer−Emmett−Teller (BET) method. Mercury porosimetry measurements were performed using an Autopore IV 9500 (Micromertitics Company).

Results and Discussions

Water is essential to photosynthesis. Large amounts of water are transpired by a tree on a daily basis. As shown in Figure 1a, water is absorbed by the root system and is transported up the tree trunks that act much like pipes to the leaves for photosynthesis. Food made in the leaves is then transported down to the roots and to other parts of the tree for growth. The trunks contain a network of tubes (Figure 1b) that runs between the roots and the leaves and acts as the central plumbing system for the tree. Tree trunk, generally spoken as wood is a natural composite and exhibits an anisotropic, 3D porous morphology. Macroscopically, wood is characterized by the formation of growth ring structures. The microstructural hierarchical features of wood range from the millimeter (growth ring structures) through the micrometer (tracheidal cell patterns, macro- and microfibril cell-wall textures) down to the nanometer scale (molecular fiber and membrane structures of cell walls (Figure 1b, 1c, 1d).[30] Wood tissue is characterized by a hierarchical anatomy of unidirectionally oriented cells. The morphology and arrangement of the cells vary between deciduous and coniferous wood. Coniferous wood has a very uniform structure (Figure 1b), it consists of 90~95% tracheids, which are long and slender cells tapered at the ends. Deciduous wood is less homogeneous (Supporting Information, Figure S2). Tracheids elements are oriented in the direction of the trunk axis. They form the transportation paths as long continuous tubes for water and minerals within the living tree (Figure 1b).

In this work, a typical coniferous wood White pine was chosen as a template. As shown in **Figure 2**a, 2b, white pine has a nearly monomodal microsized pore distribution. The mean pore diameter of the tracheids is 10 µm. The longitudinal section is composed of oriented long microtubes with a diameter of 10µm (Figure 2c, 2d). Cells arranged in radial direction (rays) and pores in the cell walls create a 3D macropore network for transportation. Furthermore, the walls of the cells are composed of numerous micropores according to the N_2 adsorption measurement (**Figure 3**a) which are from the nanosized molecular fibers. Such hierarchical porous anatomy endows the wood with high surface area up to 345 $m^2 g^{-1}$ (Figure 3a). Here, activation process was applied on the carbonized wood template to increase its surface area significantly, approaching ~1757 $m^2 g^{-1}$ (Figure 1e and 3a). Activation process causes more micropores to form and therefore a major relative increase in pore volume in the micropore range (Figure 3a). Obviously, main micropores are formed during the partial oxidation and removal of carbon in hot air, which leads to the increase of specific surface area and the porosity. Activated carbonized wood with 3D hierarchical micro/meso/macroporous anatomy and high surface area was a promising template for the synthesis of the corresponding

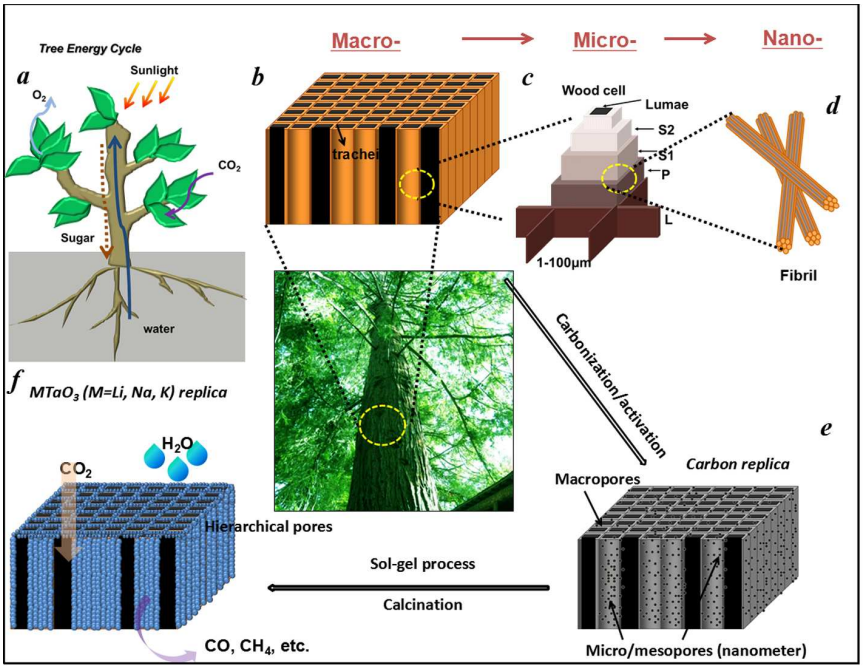

Figure 1. Schematic illustration of (a) Tree energy cycle. (b) Hierarchical macro- and (c) microscopic cell structures of tree trunks. A single longitudinal tracheidal cell exhibits a layered wall structure, a thin primary wall (P), and a thicker secondary wall composed of sublayers (S1, S2), which vary in cellulose microfibril orientation and play a key role in the mechanical behavior of cellular tissue. Adjacent tracheids are joined together by a highly lignified layer (middle lamella L). (d) The fibril structure of a cell wall showing the nanoscale. (e) Carbonization/activation process for the production of activated carbonized tree trunk templates with hierarchical pores. (f) Hierarchical porous $MTaO_3$ (M=Li, Na, K) replica obtained via sol-gel/calcination process, with the conceptual drawing of an artificial system that uses only light, water, and carbon dioxide as inputs, and produces sustainable fuels.

alkaline tantalates replica. Under vacuum infiltration conditions, it was easier for the precursor solution to infiltrate into the micro/mesopores of the carbonized samples. Since there are functional groups on the surfaces of the carbonized samples, the precursors could have interaction with the surfaces which facilitated targeted materials assembly. The major biopolymeric constituents in wood are cellulose, hemicellulose, and lignin with some additional macromolecular compounds like different kinds of fat, oil, wax, minerals, alcaloides, etc. as minor constituents. [31] According to TGA data (Supporting Information, Figure S3a), the organics could be decomposed completely around 450 °C. So after calcination at 550 °C in O_2 atmosphere for 10 h, organics could be removed completely (Supporting Information, Fig. S2) leaving crystalline tantalates $MTaO_3$ (M=Li, Na, K) as demonstrated by XRD (Fig. 3b). FESEM and TEM images show the hierarchical porous anatomy of the products. Take $NaTaO_3$ as an example, the product has very loose feature (Supporting Information, Figure S4). From the cross-section, the products have highly porous structures with pores in the range of several micrometers (Figure 2e). Longitudinally, it has tube-like structures (Figure 2f). TEM image (inset of Figure 2e) shows that the macropore networks are composed of mesoporous nanocrystalline building blocks.

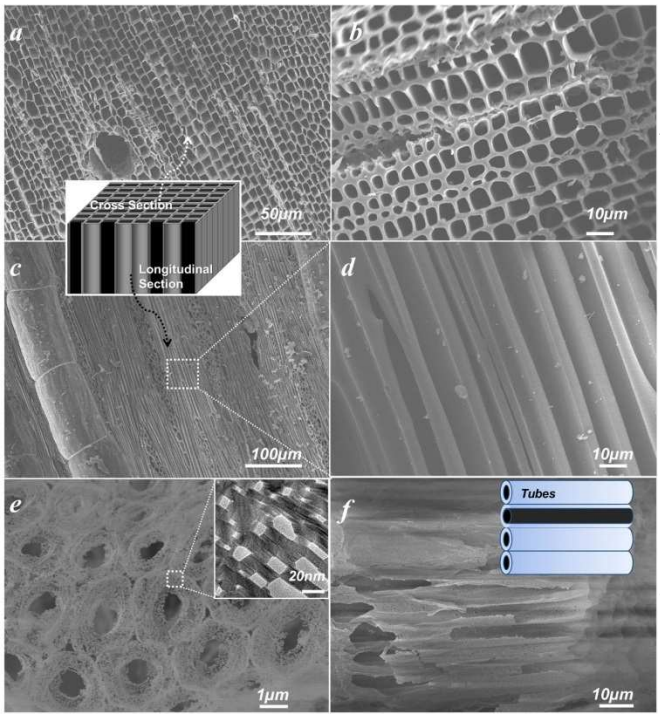

Figure 2. FESEM images of (a) the cross-section of carbonized white pine, with the inset of the 3D schematic illustration. (b) magnified image of the cross-section. (c) the longitudinal section of carbonized white pine. (d) Magnified image of the longitudinal section. (e) Porous $NaTaO_3$ replica derived from the activated carbon templates, with the inset of the corresponding TEM image, indicating the mesoporous feature. (f) FESEM image of the tubular structure of $NaTaO_3$, with the inset of the schematic illustration.

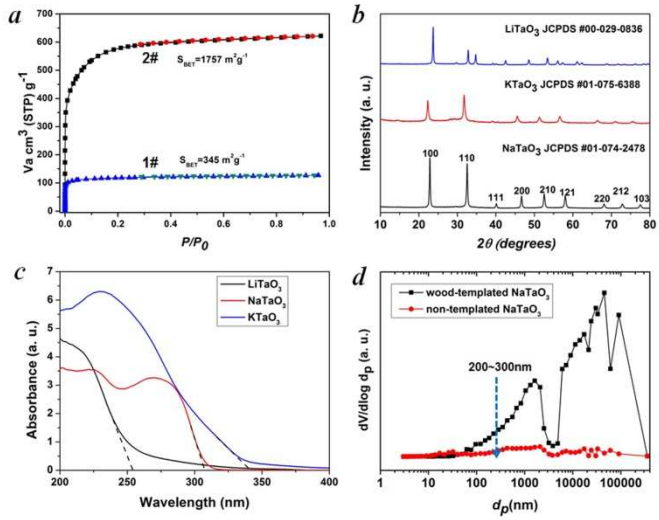

Figure 3. (a) N_2 adsorption isotherms of wood templates: 1# carbonized wood and 2# activated carbonized wood. (b) PXRD patterns of wood-templated $MTaO_3$ (M=Li, Na, K) series. (c) UV-Vis absorption spectra of wood-templated $MTaO_3$ (M=Li, Na, K) series. (d) Mercury intrusion porosimetry of $NaTaO_3$ for the characterization of hierarchical pore size distributions.

Generally, CO_2 in the presence of water vapor can be photoreduced to hydrocarbon fuels using a wide-band-gap semiconductor as a photocatalyst. [32] Because of the irradiation of full arc Xe lamp, the existed form of water for the reaction is vapor. Theoretically, alcohol or methanol could serve as electron donors to increase the activities. However, because of the well-known process Photocatalytic Reforming of Ethanol, in the presence of alcohol, the produced CO and CH_4 could increase significantly which is derived from the photocatalytic reforming of ethanol. Thus, it is not easy to analyze the carbon sources of CO and CH_4. According to the diffuse reflection spectra of alkali tantalates (Figure 3c), the onsets of the absorption of $LiTaO_3$, $NaTaO_3$ and $KTaO_3$ were 256, 310 and 344 nm. So the band gaps of $LiTaO_3$, $NaTaO_3$ and $KTaO_3$ were estimated to be 4.8, 4.0 and 3.6 eV, respectively. Here we performed artificial photosynthesis of the CO_2 + gaseous H_2O reaction in a gas−solid system over the $MTaO_3$ series. Take $NaTaO_3$ as an instance, bare $NaTaO_3$ evolve CO and CH_4 as the main products in the absence of any sacrificial agents (**Figure 4**a, 4b). It is well known that the CO_2 photoreduction mainly undergoes two courses, including oxidation and reduction processes. In the oxidation process, the photogenerated holes in the valence band oxidize water to generate hydrogen ions *via* the half-reaction ($2H_2O + 4h^+ \rightarrow O_2 + 4H^+$). In the reduction course, there is a chain reaction to reduce CO_2 to CH_4 ($CO_2 + 2H^+ + 2e^- \rightarrow CO + H_2O$, $CO_2 + 4H^+ + 4e^- \rightarrow HCHO + H_2O$, $CO_2 + 6H^+ + 6e^- \rightarrow CH_3OH + H_2O$, $CO_2 + 8H^+ + 8e^- \rightarrow CH_4 + 2H_2O$) [32]. The edges of the valence band (E_{VB}) and conduction band (E_{CB}) of $NaTaO_3$ are determined to be 2.993 and -1.007 V (vs normal hydrogen electrode, NHE) *via* the Mulliken electronegativity method, respectively.[33] E_{VB} of $NaTaO_3$ is more

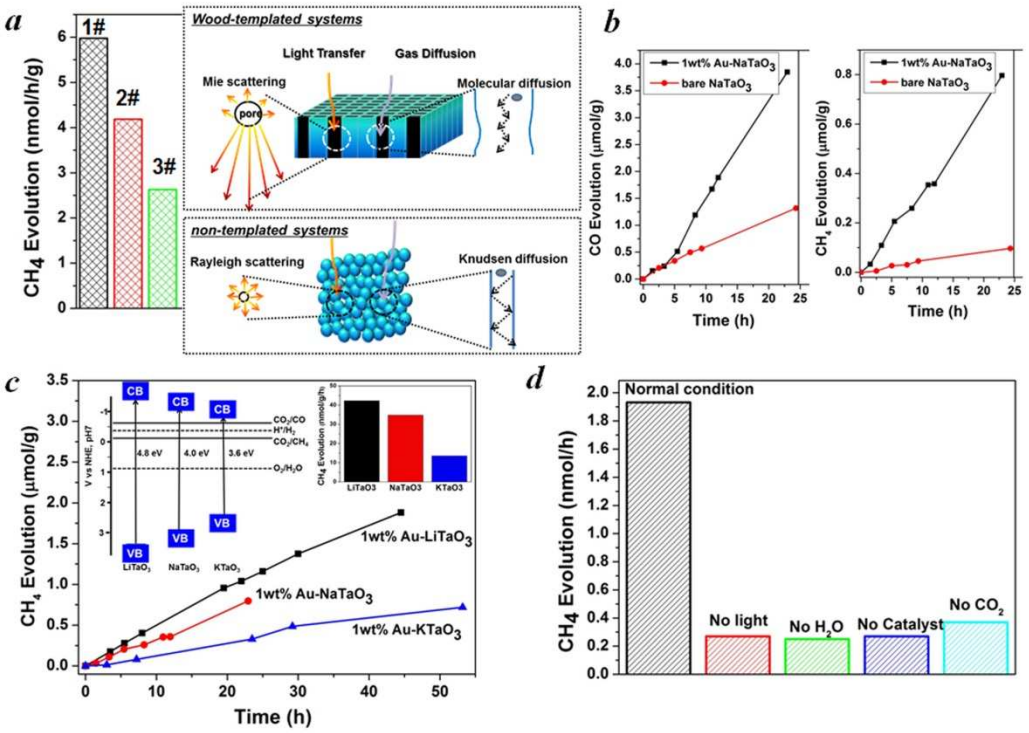

Figure 4. Photocatalytic CO_2 reduction activities. (a) Left part: CH_4 evolution on bare $NaTaO_3$ series, right part: schematic illustration of light transfer and gas diffusion in wood-templated hierarchical porous systems and non-templated systems, respectively. 1# $NaTaO_3$ derived from activated carbonized wood, 2# $NaTaO_3$ derived from carbonized wood, 3# non-templated $NaTaO_3$. (b) CO and CH_4 evolution on $NaTaO_3$ with and without loading with Au cocatalysts. (c) Photocatalytic formation of CH_4 on $MTaO_3$ (M=Li, Na, K) series derived from activated carbonized wood after loading with 1wt% Au as a cocatalyst, with the inset of the energy band structure of $MTaO_3$ (M=Li, Na, K) (d) CH_4 evolution in reference experiments in the conditions without H_2O, CO_2, light irradiation, and catalyst compared with that in normal conditions. Au (1wt %)-$NaTaO_3$ derived from activated carbonized wood was measured as the normal condition.

positive than that of E°(H_2O/H^+) ($H_2O \rightarrow 1/2O_2 + 2H^+ + 2e^-$, E° redox = 0.82 V vs NHE), and E_{CB} is more negative than that of E° (CO_2/CO) ($CO_2 + 2e^- + 2H^+ \rightarrow CO + H_2O$, E° redox = -0.53 V vs NHE) and E° (CO_2/CH_4) ($CO_2 + 8e^- + 8H^+ \rightarrow CH_4 + 2H_2O$, E° redox = -0.24 V vs NHE). This indicates that the photogenerated electrons and holes on the irradiated $NaTaO_3$ can react with adsorbed CO_2 and H_2O to produce CO and CH_4. Other products such as HCOOH, HCHO, CH_3OH were not detected, probably because for the gas-phase CO_2 photoreduction with low proton concentrations, CO is the primary first step product instead of HCOOH [34-36]. The intermediates produced during the reduction tend to favor the formation of CH_4 instead of CH_3OH, HCHO and HCOOH [34-36]. Furthermore, the strong oxidation power of photogenerated holes (or OH radicals) that can react with intermediates and products of CO_2 conversion in reactions, [34-36] making the net yield negligible. It is also worth mentioning that in our semiconductor systems, there was no H_2 detected, probably because in the absence of sacrificial agents in our system, the produced H_2 was served as reductants for CO_2 photoreduction.

Hierarchical porous anatomy could influence their activity. Take $NaTaO_3$ as an instance, activated carbonized wood-templated $NaTaO_3$ exhibits about a 2.23-fold improvement in activities than non-templated $NaTaO_3$ based on the same amount (Figure 4a) mainly due to the enhanced light transfer and faster gas diffusion. Hendricks and Howell [37] indicate that the porous structure of ceramics creates complex electromagnetic scattering and interference patterns within the structure. Particularly, when the size of the voids is comparable to the wavelength of the incident light, the Mie's scattering happens in which the light scatters strongly along the forward direction. This scattering produces a pattern like an antenna lobe, with a sharper and more intense forward lobe (Figure 4a, right part). [38] According to the diffuse reflection spectra and the spectrum of Hg-Xe lamp (Supporting Information, Figure S5), the effective incident light wavelength is between 200~310nm. According to the mercury porosimeter (Figure 3d), the quantity of macropores around 200~310nm comparable with the incident light wavelength in wood-templated $NaTaO_3$ are obviously much more than that of non-templated $NaTaO_3$. Therefore, the path length of the incident light is increased, [39] leading to a promoted light utilization efficiency. The scattered light then transfers to and is absorbed by the neighbored pores, thus inducing more photo-excited electrons for the reduction (Figure 4a, right part).

On the other hand, gas diffusivity is another key factor. When the diameter of the pore is much greater than the mean free path of the gas molecules, the diffusing molecules will interact with each other more than with the pore walls, thereby minimizing the wall effects on the transport [40]. In our case, the mean free paths of CO_2, CH_4, CO and H_2O were calculated to be about 74, 70, 72 and 139 nm according to Equation (1), respectively. Where K equals to 1.38×10^{-23}, T is assumed to be 323K in our experiment, D_0 refers to the diameters of gas molecules (nm).

$$L = \frac{KT}{\sqrt{2}\pi D_0^{\,2} P} \quad (1)$$

According to the SEM and mercury porosimeter, a number of macropores are in the range of several to hundreds of micrometers, thus the pore diffusivity is essentially the same as the molecular diffusivity, in which the diffusion coefficient is much larger than that in mesopores (Figure 4a, right part). Contrastly, the gas diffusion in non-templated system with much fewer and smaller pores is mainly Knudsen diffusion where the gas molecules collide with the pore walls frequently (Figure 4a, right part). Thus, the gas diffusion rate is smaller and longer time is required for reactants to move into the deeper as well as for products to move from the deeper layer into the atmosphere. The higher activity of activated carbonized wood-templated system (Figure 4a, 1#) than carbonized wood-templated system (Figure 4a, 2#) are mainly because of higher surface areas and higher volume of mesopores derived from the porous activated carbon templates, (Supporting Information, Table S1) provide more reaction sites, thus enhancing the overall performances.

The evolution rates of CO and CH_4 over $NaTaO_3$ could be significantly enhanced by a factor of 3.1 and 8.4, respectively after loading Au cocatalyst to facilitate the proton-coupled multielectron transfer (Figure 4b). A precipitation method was used for the deposition of Au nanoparticles. XPS spectrum (Supporting Information, Figure S6) demonstrates the metallic Au formation. The size of Au is only about 3 nm (Supporting Information, Figure S7) with good homogeneity, which coincides with other's reports. [41]After loading with about 1wt% Au onto $MTaO_3$ series, the activities were in the order of $LiTaO_3$ > $NaTaO_3$ > $KTaO_3$ as compared in Figure 4c. According to the Mulliken electronegativity method [33], the edges of the conduction band of $LiTaO_3$, $NaTaO_3$, $KTaO_3$ were estimated to be -1.302V, -1.007 V and -0.98 V (vs NHE) respectively (inset of Figure 4c). The order of the photocatalytic activities was consistent with that of the conduction band levels, indicating wide band gap semiconductors with higher reduction potentials are more favorable for CO_2 photo-fixation. We compared our results with other photocatalytic systems with respect to efficiency and selectivity, and the data is shown in Table 1. But since the experimental conditions (light intensity, irradiation distance, catalysts amount, and others) are different, so it may be not suitable for comparison. Here we also compared our

Table 1. Comparison with other photocatalytic systems.

Light source	Catalyst	Co-catalyst	Reaction medium	Products	$Sel._{CH4}$[a]/%	Ref
300 W Xe lamp	Leaf-architectured $SrTiO_3$	1 wt % Au	CO_2 and H_2O vapor	CO (350 nmol/h/g) CH_4 (275 nmol/h/g)	44.1	[46]
UV Xe lamp	TiO_2 rods with {010} facets	1 wt % Pt	CO_2 and H_2O vapor	CH_4 (5.7 μmol/h/g)	100	[47]
300 W Xe lamp UV	hollow anatase TiO_2 single crystals with {101} facets	1 wt % RuO_2	CO_2 and H_2O vapor	CH_4 (1.725 μmol/h/g)	100	[48]
350 W Xe lamp UV	SiO_2-Pillared HNb_3O_8	0.4 wt % Pt	CO_2 and H_2O vapor	CH_4 (2.9 μmol/h/g)	100	[49]
300 W Xe arc lamp visible light λ >420 nm	$Na_2V_6O_{16}$ nanoribbons	1 wt % Pt and 1 wt% RuO_2	CO_2 and H_2O vapor	CH_4 (190 nmol/h/g)	100	[50]
Xe arc lamp visible light λ >420 nm	$W_{18}O_{49}$ nanowires	—	CO_2 and H_2O vapor	CH_4 (666 ppm/h/g)	100	[21]
visible light λ >420 nm	$ZnAl_2O_4$-modified mesoporous ZnGaNO	0.5 wt % Pt	CO_2 and H_2O vapor	CH_4 (9.2 μmol/h/g)	100	[51]
Xe lamp UV	Zn_2GeO_4 nanobelts	1 wt % Pt and 1 wt % RuO_2	CO_2 and H_2O vapor	CH_4 (25 μmol/h/g)	100	[10]
300 W Xe arc lamp visible light λ >420 nm	sheaf-like, hyperbranched $Zn_{1.7}GeN_{1.8}O$	1 wt % Pt and 1 wt % RuO_2	CO_2 and H_2O vapor	CH_4 (9 μmol/h/g)	100	[52]
200 W Hg-Xe arc lamp	$NaTaO_3$	1 wt % Au	CO_2 and H_2O vapor	CO (173 nmol/h/g) CH_4 (36 nmol/h/g)	17.3	This work

[a] $Sel._{CH4}$/%= mol(CH_4)/mol (CH_4+CO).

photocatalytic systems with some typical semiconductors (published by our group) measured with the same reactor system (Table S2).

For all samples, there is no oxygen detected. Water oxidation is much more difficult kinetically and energetically than H_2 evolution, requiring large overpotential. The oxygen generated by the water oxidation is partially used for the oxidation of the evolved products (HCOOH, HCHO, CO, etc.) [42] On the other hand, O_2 evolution is controlled by the interfacial reaction so that the semiconductor should provide a favorable reaction site for O_2 formation process. If not so, O_2 is easy to be absorbed on the surface oxygen vacancies [43] and more undesirably absorbs electrons to form O^-_2 or other species such as H_2O_2 that chemisorbs on the surfaces of catalysts and can rise the redox energy of half-reaction, making the necessary overvoltage still larger [44], thus further inhibit O_2 production. We checked the XRD patterns before and after irradiation on wood-templated NaTaO3 (Figure S8) to check the chemical stability. Furthermore, Figure 4b and 4c show that after long term irradiation (24h~54h), the activities of $MTaO_3$ (M=Li, Na, K) series kept almost linear, which further demonstrate the stability of these catalysts. Finally, to confirm that the hydrocarbon fuels were generated from the reduction of CO_2 *via* the protons released from H_2O oxidization and photogenerated electrons, control experiments were carried out as shown in Figure 4d. When the experiment was carried out in the absence of H_2O, catalyst or light irradiation, very little CH_4 was detected due to the 1 ppm of CH_4 as the contamination from air during samplings. In the case that the CO_2 gas was replaced by Ar gas, a small amount of CH_4 was found which should be generated from the photoreduction of the remaining CO_2 on the sample surface [45].

Conclusions

To conclude, we have successfully synthesized alkaline tantalates $MTaO_3$ (M=Li, Na, K) with hierarchical porous anatomy *via* the development of a general approach using activated carbonized tree trunks as templates. CO_2 photo-fixation processes indicate that H_2O supplies protons, CO_2 offers a carbon source, and the photocatalyst gives the redox potentials for the whole reaction to finally produce CO and CH_4. The research opens a new pathway for the oriented design, controlled synthesis and application of 3D hierarchical porous systems for the realization of artificial photosynthesis, especially for gas-solid reactions. The work predicts that activated carbonized biomass with rather high surface area and high hierarchical pore volume could be promising models for the design and fabrication of a new class of hierarchical catalysts for improved performance. Similar strategy could be extended to a wide range of multi-metallic catalysts. Since natural patterns and shapes arise in innumerable ways on a range of scales, our results suggest that the discovery of topological morphologies associated with photosynthesis is of great significance and the unique morphologies models are promising for the biomimetic synthesis of artificial analogues. Moreover, the research would provide a conceptual blueprint for the ultimate construction towards "artificial trees" and envisions creating "forests" of these carbon-capturing artificial trees for large scale CO_2 photo-fixation into sustainable fuels. Finally, we anticipate that this concept may be of interest to a variety of energy capture, conversion and storage areas, and may also result in significant improvements in various applications, ranging from solar cells, fuels cells and lithium-based battery.

Notes and references

[a] *International Center for Materials Nanoarchitectonics (WPI-MANA) and Environmental Remediation Materials Unit, National Institute for Materials Science (NIMS), 1-1, Namiki, Tsukuba, Ibaraki 305-0044, Japan*
E-mail: Jinhua.YE@nims.go.jp
[b] *Graduate School of Chemical Sciences and Engineering, Hokkaido University, Sapporo, Japan*
[c] *TU−NIMS Joint Research Center, School of Materials Science and Engineering, Tianjin University, 92 Weijin Road, Nankai District, Tianjin 300072, P. R. China*
[d] *State Key Lab of Metal Matrix Composites, Shanghai Jiaotong University, Shanghai, 200240, China*

† Electronic Supplementary Information (ESI) available: [FESEM images, TGA curves, XPS spectrum, TEM image, the spectrum of the lamp, Reaction setup]. See DOI: 10.1039/b000000x/
‡ Footnotes should appear here. These might include comments relevant to but not central to the matter under discussion, limited experimental and spectral data, and crystallographic data.

ACKNOWLEDGMENT

We are grateful for financial support by the World Premier International Research Center Initiative on Materials Nanoarchitectonics, MEXT, Japan and the National Natural Science Foundation of China (51102163).

1 Lewis, N. S.; Nocera, D. G.;, *Proc. Natl. Acad. Sci. USA* **2006**, 103, 15729–15735.
2 Michl, J.; *Nat. Chem.* **2011**, 3, 268–269.
3 Bensaid, S.; Centi, G.; Garrone, E.; Perathoner, S.; Saracco, G.; *ChemSusChem* **2012**, 5, 500–521.
4 M. Antonietti, *Angew. Chem. Int. Ed.* **2013**, 52, 1086–1087.
5 Liu, J.; Antonietti, M.; *Energy Environ. Sci.,* **2013**, 6, 1486-1493.
6 Halmann, M.; *Nature* **1978**, 275, 115–116.
7 Roy, S. C.; Varghese, O. K.; Paulose, M.; Grimes, G. A.; *ACS Nano* **2010**, 4, 1259–1278.
8 Navalon, S.; Dhakshinamoorthy, A.; Alvaro, M.; Garcia, H.; *ChemSusChem*, **2013**, 6, 562-577.
9 Hoffmann, M. R.; Moss, J. A.; Baum, M. M.; *Dalton Trans.* **2011**, 40, 5151.
10 Liu, Q.; Zhou, Y.; Kou, J.; Chen, X.; Tian, Z.; Gao, J.; Yan, S.; Zou, Z. G.; *J. Am. Chem. Soc.* **2010**, 132, 14385–14387.
11 Zhang, N.; Ouyang, S. X.; Li, P.; Zhang, Y. J.; Xi, G. C.; Kako, T.; Ye, J. H.; *Chem. Commun.* **2011**, 47, 2041–2043.
12 Yan, S. C.; Ouyang, S. X.; Gao, J.; Yang, M.; Feng, J. Y.; Fan, X. X.; Wan, L. J.; Li, Z. S.; Ye, J. H.; Zhou, Y.; Zou, Z. G.; *Angew. Chem. Int. Ed.* **2010**, 49, 6400–6404.
13 Yan, S. C.; Wang, J. J.; Gao, H.; Wang, N.; Yu, H.; Li, Z.; Zhou, Y.; Zou, Z.; *Adv. Func. Mater.* **2013**, 23, 758-763.
14 Li, P.; Ouyang, S.; Xi, G.; Kako, T.; Ye, J.; *J. Phys. Chem. C*, **2012**, 116, 65-70.
15 Li, Z.; Zhou, Y.; Zhang, J.; Tu, W.; Liu, Q.; Yu, T.; Zou, Z.; *Crystal Growth &Design*, **2012**, 12, 1476-1481.
16 Cheng, H.; Huang, B.; Liu, Y.; Wang, Z.; Qin, X.; Zhang, X.; Dai, Y.; *Chem. Commun.* **2012**, 48, 9729-9731.
17 Zhou, Y.; Tian, Z.; Zhao, Z.; Liu, Q.; Kou, J.; Chen, X.; Gao, J.; Yan, S.; Zou, Z.; *ACS Appl. Mater. Interfaces*, **2011**, 3, 3594-3601.
18 Osterloh, F. E.; *Chem. Mater.* **2008**, 20, 35–54.
19 Chen, X.; Shen, S.; Guo, L.; Mao, S. S.; *Chem. Rev.* **2010**, 110, 6503–6570.
20 Tong, H.; Ouyang, S. X.; Bi, Y. P.; Umezawa, N.; Oshikiri, M.; Ye, J. H.; *Adv. Mater.* **2012**, 24, 229–251.

21 Xi, G. C.; Ouyang, S. X.; Li, P.; Ye, J. H.; Ma, Q.; Su, N.; Bai, H.; Wang, C.; *Angew. Chem. Int. Ed.* **2012**, 51, 2395–2399.

22 Liu, J.; Cazelles, R.; Chen, Z. P.; Zhou, H.; Galarneau, A.; Antonietti, M.; *Phys. Chem. Chem. Phys.*, **2014**, 16, 14699-14705.

23 Tu, W.; Zhou, Y.; Liu, Q.; Tian, Z.; Gao, J.; Chen, X.; Zhang, H.; Liu, J.; Zou, Z.; *Adv. Func. Mater.* **2012**, 22, 1215-1221.

24 In, S.; Vaughn, D. D.; Schaak, R. E.; *Angew. Chem. Int. Ed.* **2012**, 51, 3915-3918.

25 Varghese, O. K.; Paulose, M.; Latempa, T. J.; Grimes, C. A.; *Nano Lett.* **2009**, 9, 731-737.

26 Fu, Y.; Sun, D.; Chen, Y.; Huang, R.; Ding, Z.; Fu, X.; Li, Z.; *Angew. Chem. Int. Ed.* **2012**, 51, 3364-3367.

27 Mitchell, S.; Michels, N. L.; Kunze, K.; Ramirez, J. P.; *Nature. Chem.* **2012**, 4, 825-831.

28 Li, Y.; Fu, Z. Y.; Su, B-L.; *Adv. Func. Mater.*, **2012**, 22, 4634-4667.

29 H. Zhou, X. F. Li, T. X. Fan, F. E. Osterloh, J. Ding, E. M. Sabio, D. Zhang, Q. X. Guo, *Adv. Mater.* **2010**, 22, 951-956.

30 Sieber, H.; Hoffmann, C.; Kaindl, A.; Greil, P.; *Adv. Eng. Mater.* , **2000**, 2, 105-109.

31 Greil, P.; *J. Eur. Ceram. Soc.* **2001**, 21, 105-118.

32 Inoue, I.; Fujishima, A.; Konishi, S.; Honda, K.; *Nature* **1979**, 277, 637–638.

33 Butler M. A.;Ginley, D. S.; *J. Electrochem. Soc.*, **1978,** 125, 228.

34 Kumar, B.; Llorente, M.; Froehlich, J.; Dang, T.; Sathrum, A.; Kubiak, C. P.; *Annu. Rev. Phys. Chem.* **2012**, 63, 541-569

35 Peterson, A. A.; Pedersen, F. A.; Studt, F.; Rossmeisl, J.; Norskov, J. K.; *Energy Environ. Sci.*, **2010**, 3, 1311-1315.

36 Halasi, G.; Schubert, G.; Solymosi, F.; *J. Phys. Chem. C* **2012**, 116, 15396–15405.

37 Hendricks T. J.; Howell, J. R.; *J. Heat Transfer* 1996, 118, 911–917.

38 Mie, G.; *Ann. Phys.* 1908, 330, 377−445.

39 Koo, H. J.; Park, J.; Yoo, B.; Yoo, K.; Kim, K.; Park, N. G.; *Inorg. Chim. Acta* 2008, 361, 677−683.

40 Cindrella, L.; Kannan, A. M.; Lin, J. F.; Saminathan, K.; Ho, Y.; Lin, C. W.; Wertz, J.; *J. Power Sources* 2009, 194, 146–160.

41 Silva, C. G.; Juarez, R.; Marino, T.; Molinari, R.; Garcia, H.; *J. Am. Chem. Soc.* 2011, 133, 595–602.

42 Gorem, Z.; Willner, I.; Nelson, A. J.; Frank, A. J.; *J. Phys. Chem.* 1990, 94, 3784–3790.

43 Lira, E.; Wendt, S.; Huo, P.; Hansen, J.; Streber, R.; Porsgaard, S.; Wei, Y.; Bechstein, R.; Lagsgaard, E.; Besenbacher, F.; *J. Am. Chem. Soc.* 2011, 133, 6529–6532.

44 Salvador, P.; Gutierrez, C.; *Surface Science*, 1983, 124, 398-406.

45 Dimitrijevic, N. M.; Vijayan, B. K.; Poluektov, O. G.; Rajh, T.; Gray, K. A.; He, H.; Zapol, P.; *J. Am. Chem. Soc*. 2011, 133, 3964–3971.

46 Zhou, H.; Guo, J.; Li, P.; Fan, T. X.; Zhang, D.; Ye, J. H.; *Scientific Reports*, 2013, 2, 1667.

47 Pan, J.; Wu, X.; Wang, L.; Liu, G.; Lu, G. Q.; Cheng, H. M. ; *Chem Commun.*, 2011, 47(29): 8361-8363.

48 Jiao, W.; Wang, L.; Liu, G.; Lu, G. Q.; Cheng, H. M.; *ACS Catalysis*, 2012, 2(9): 1854-1859.

49 Li, X.; Li, W.; Zhuang, Z.; Zhong, Y.; Li, Q.; Wang, L.; *J. Phys. Chem. C*, 2012, 116(30): 16047-16053.

50 Feng, S.; Chen, X.; Zhou, Y.; Tu, W.; Li, P.; Li, H.; Zou, Z.; *Nanoscale*, 2014, 6(3): 1896-1900.

51 Yan, S.; Yu, H.; Wang, N.; Li, Z.; Zou, Z.; *Chem Commun.*, 2012, 48(7): 1048-1050.

52 Liu, Q.; Zhou, Y.; Tian, Z.; Chen, X.; Gao, J.; Zou, Z.; *J. Mater. Chem.*, 2012, 22(5): 2033-2038.